

Design Methodology of LLC Resonant Converters for Electric Vehicle Battery Chargers

Junjun Deng, *Student Member, IEEE*, Siqi Li, Sideng Hu, Chunting Chris Mi, *Fellow, IEEE*, and Ruiqing Ma, *Member, IEEE*

Abstract—In this paper, an inductor–inductor–capacitor (LLC) resonant dc–dc converter design procedure for an onboard lithium-ion battery charger of a plug-in hybrid electric vehicle (PHEV) is presented. Unlike traditional resistive load applications, the characteristic of a battery load is nonlinear and highly related to the charging profiles. Based on the features of an LLC converter and the characteristics of the charging profiles, the design considerations are studied thoroughly. The worst-case conditions for primary-side zero-voltage switching (ZVS) operation are analytically identified based on fundamental harmonic approximation when a constant maximum power (CMP) charging profile is implemented. Then, the worst-case operating point is used as the design targeted point to ensure soft-switching operation globally. To avoid the inaccuracy of fundamental harmonic approximation approach in the below-resonance region, the design constraints are derived based on a specific operation mode analysis. Finally, a step-by-step design methodology is proposed and validated through experiments on a prototype converting 400 V from the input to an output voltage range of 250–450 V at 3.3 kW with a peak efficiency of 98.2%.

Index Terms—Battery charger, DC–DC converter, electric vehicle (EV), LLC resonant converter, plug-in hybrid EV(PHEV), zero-current switching (ZCS), zero-voltage switching (ZVS).

I. INTRODUCTION

RECENTLY, there is a growing interest in plug-in hybrid electric vehicles (PHEVs) and pure electric vehicles (EVs) because of the threat of fossil fuel depletion and global warming [1]–[4]. Most current PHEVs and EVs are equipped with a lithium-ion battery pack. A single-phase 3–6 kW onboard charger is usually installed on passenger cars, and a three-phase 30–200 kW battery charger is installed for buses and trucks; therefore, the high power traction battery pack can be charged through a utility power outlet [5].

High-voltage, high-current, and sophisticated charging algorithms are involved in quick charging of high-capacity lithium-

Manuscript received July 22, 2013; revised October 7, 2013; accepted October 19, 2013. Date of publication October 25, 2013; date of current version May 8, 2014. The review of this paper was coordinated by Prof. A. Khaligh.

J. Deng is with the School of Automation, Northwestern Polytechnical University, Xi'an 710072, China, and also with the Department of Electrical and Computer Engineering, University of Michigan, Dearborn, MI 48109 USA (e-mail: dengjunjun1985@gmail.com).

S. Li, S. Hu, and C. C. Mi are with the Department of Electrical and Computer Engineering, University of Michigan, Dearborn, MI 48109 USA (e-mail: lisiqi00@gmail.com; husideng@gmail.com; mi@ieee.org).

R. Ma is with the School of Automation, Northwestern Polytechnical University, Xi'an 710072, China (e-mail: marq@nwpu.edu.cn).

Color versions of one or more of the figures in this paper are available online at <http://ieeexplore.ieee.org>.

Digital Object Identifier 10.1109/TVT.2013.2287379

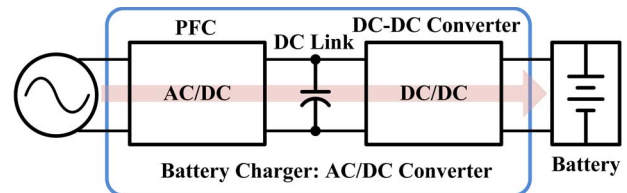


Fig. 1. Typical power architecture of a battery charger.

ion battery packs [6]. Moreover, high efficiency with high power density, high reliability, small size, and low cost are the basic requirements for an onboard charger. All these factors make the design of an onboard charger complicated and costly, which has been regarded as one of the barriers that keeps PHEVs from wide acceptance [5].

The size, cost, and mechanical packaging are well discussed from a practical aspect in [6] and [7]. A comprehensive topological survey of the currently available charging solutions has also been presented in [8] and [9]. The most common charger architecture consists of a boost-type ac–dc converter for active power factor correction, and an isolated dc–dc converter as the second stage [6], as shown in Fig. 1. The characteristic of this type of charger is mainly dependent on the dc–dc stage since the output voltage and current are regulated in this stage [10], [11]. Among different solutions, an inductor–inductor–capacitor (LLC) resonant converter becomes the most attractive topology due to its high efficiency, low electromagnetic interference (EMI) emissions, a wide operation range, and the ability to achieve high power density [12]. Such features excellently fit the demand of PHEV and EV charger applications. However, the LLC topology is difficult to analyze and design because of its multiple resonant components and various operation modes [13].

Many design methodologies have been proposed for this type of converter in the past decades. Exact analysis of LLC resonant converters [14] ensures accuracy but cannot be easily used to get a handy design procedure due to the complexity of the model. The methodologies based on first harmonic approximation (FHA) analysis [15], [16] are much simpler to handle. The FHA approach gives acceptable accurate results for operating points at and above the resonance frequency of the resonant tank [17]. Therefore, it has been widely used in constant output voltage applications where the LLC converter is designed to resonate at nominal condition. Designing a wide-output-range LLC resonant converter based on FHA is investigated in [18], and the expanded range is mainly designed in frequencies above the resonant frequency. However, zero-current switching (ZCS) for output rectifier diodes is lost in this region, which causes

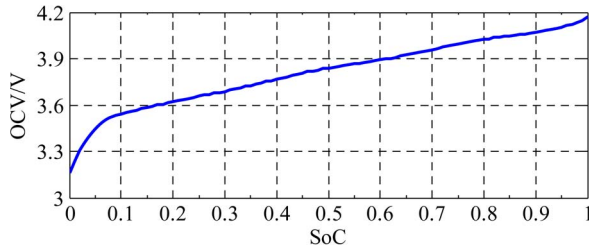


Fig. 2. Relationship between battery OCV and SOC for a single lithium-ion battery cell.

additional diode reverse recovery losses compared with the region below resonance [19]. The FHA is still valid but less accurate in the below-resonance region; therefore, it is useful for qualitative analysis but not for optimal design procedure. Optimal design methods are developed based on the operation mode analysis in [20] and [21]. These approaches can give quite good design results but call for utilizing sophisticated calculation tools. A simple yet accurate design-oriented model and a step-by-step design procedure that ensure most merits of an LLC converter are presented in [22], but the wide output voltage range has not been discussed.

In the previous studies, the load is usually assumed to be a resistor. Taking the characteristics of lead–acid batteries into account, a design procedure and practical design considerations for the LLC converter in battery charger applications are presented in [23]. The optimization of burst-mode operation for occasionally deep discharged lead–acid battery pack has been discussed in [24]. However, the characteristic of lithium-ion battery load and its impact on the design of LLC converter are not well researched. For a high-voltage lithium-ion battery charger, the design requirements are greatly different and challenging compared with passive load applications and lead–acid battery applications.

First of all, nonlinear load I – V characteristics exist in the design of a resonant converter for battery charger applications. The properties of the resonant converter are nonlinearly affected by the load current [25]. For an LLC converter connected with a passive load, the output voltage is largely determined by the load current, whereas for battery load, the output voltage is related to the battery state-of-charge (SOC) and the charging profile. The nonlinear properties affected by nonlinear load make it harder to frame design constraints and objects into the design procedure.

Second, the load voltage significantly varies in the whole charging process. The voltage range of a single cell lead–acid battery is generally 1.75–2.4 V. By contrast, for a single-cell lithium-ion battery (4.2 V/cell), the open-circuit voltage (OCV) increment could be more than 1 V per cell as the SOC reaches the full level from zero, as shown in Fig. 2 [26]. This means that there is nearly a 100-V increment for a battery package applied for a 400-V PHEV drive system. As a result, the LLC converter should be able to handle a widely adjustable regulated output voltage range even when the load current varies. Moreover, lithium-ion battery has better weight-to-energy density ratio, which calls for higher power rating requirements for the chargers.

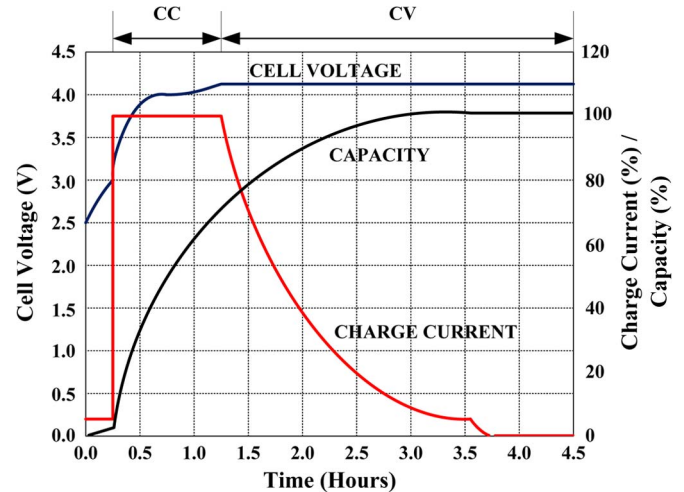


Fig. 3. Charge profile for a single lithium-ion battery cell.

Third, the charge process for a lithium-ion battery usually contains two main stages: a constant-current (CC) charging stage and a constant-voltage (CV) charging stage, as shown in Fig. 3. Moreover, a trickle charging stage before the CC stage is necessary for deeply depleted cells [27]. The design requirements are not the same in the different stages. For the benefits of saving charging time, in the CC charging stage, a preset maximum charging current is controlled by the charger while monitoring the battery voltage. In the trickle charging stage or the CV charging stage, the charge current is much smaller than that in the CC stage. Hence, the light-load efficiency and overcharging issues are more critical in this stage.

Based on the given analysis, the design requirements for an LLC-resonant-converter-based PHEV lithium-ion battery charger are significantly different from those for regular passive load applications. In this paper, some general design guidelines for resistive load are discussed based on the FHA analysis of the LLC converter in Section II. The impacts of battery load characteristics that relate to the charging profiles on the design considerations of LLC converters are investigated in Section III. The design constraints for realizing soft-switching under all operating conditions are derived in Section IV. Then, the design procedure is proposed in Section V. Experimental results are presented in Section VI, and conclusions are drawn in Section VII.

II. MAIN FEATURES OF LLC RESONATE CONVERTERS

The LLC topology can be implemented as a half-bridge type or a full-bridge type. The full-bridge type is preferable in PHEV charger applications due to its high power rating. A typical schematic of a full-bridge LLC multiresonant dc–dc converter is shown in Fig. 4, where C_r is the resonant capacitor, L_m is the magnetizing inductor, and L_r is the leakage inductor reflected in the primary side. These reactive components form the resonant tank. In the switch network shown in Fig. 4, S_1 and S_4 , and S_2 and S_3 are grouped, respectively. Each group is turned on and off with a 50% duty cycle at frequency f_s with 180° out-of-phase between groups, to generate a symmetrical square waveform with amplitude V_{in} , as shown in Fig. 5. This

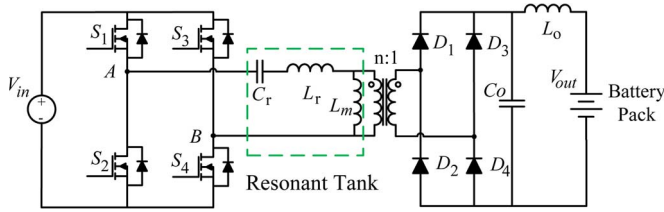


Fig. 4. LLC resonant full-bridge converter.

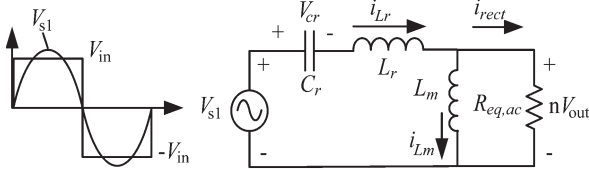


Fig. 5. AC equivalent circuit of the LLC resonant converter.

voltage is applied to the resonant tank so that energy can be transferred to the load, which is coupled to the resonant tank by an ideal transformer [28].

The ac equivalent circuit of an LLC resonant converter based on FHA analysis is shown in Fig. 5. In this circuit, $R_{eq,ac}$ is equivalent to the load and rectifier stage defined as follows [6], [18], [25], [29]:

$$R_{eq,ac} = n^2 \frac{8}{\pi^2} \frac{V_{out}}{I_{out}} = n^2 \frac{8}{\pi^2} \frac{V_{out}^2}{P_{out}} \quad (1)$$

where n is the transformer turns ratio between the primary side and the secondary side, and V_{out} , I_{out} , and P_{out} denote the output voltage, current, and power, respectively. In addition, the output voltage is clamped by the battery and is considered the same while the charging is carried out.

The dc voltage gain of LLC converters is obtained based on FHA equivalent circuit analysis [17], i.e.,

$$M(f_n, l, Q) = \frac{1}{\sqrt{\left(1 + l - \frac{l}{f_n^2}\right)^2 + Q^2 \cdot \left(f_n - \frac{1}{f_n}\right)^2}} \quad (2)$$

with the following parameter definitions:

$$\text{voltage conversion ratio: } M = \frac{nV_{out}}{V_{in}}$$

$$\text{resonance frequency: } f_{r1} = \frac{1}{2\pi\sqrt{L_r C_r}}$$

$$\begin{aligned} \text{characteristic impedance: } Z_0 &= \sqrt{\frac{L_r}{C_r}} \\ &= 2\pi f_{r1} L_r = \frac{1}{2\pi f_{r1} C_r} \end{aligned}$$

$$\begin{aligned} \text{quality factor: } Q &= \frac{Z_0}{R_{eq,ac}} = \frac{\pi^2}{8} \frac{I_{out}}{V_{out}} \frac{1}{n^2} Z_0 \\ &= \frac{\pi^2}{8} \frac{P_{out}}{(nV_{out})^2} Z_0 \end{aligned}$$

$$\text{inductance ratio: } l = \frac{L_r}{L_m}$$

$$\text{normalized frequency: } f_n = \frac{f_s}{f_{r1}}$$

where f_s in the last definition denotes the switching frequency.

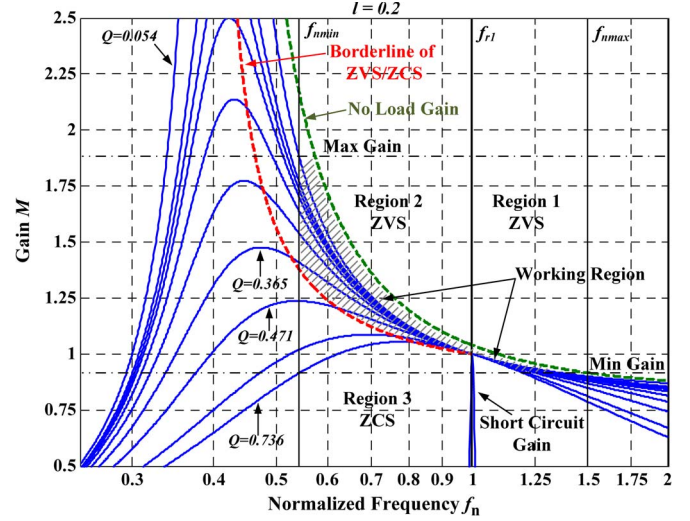


Fig. 6. DC gain characteristics of the LLC resonant converter based on FHA.

The normalized input impedance of the resonant tank can be derived as follows:

$$\begin{aligned} Z_n(f_n, l, Q) &= \frac{Z_{in}(f_n, l, Q)}{Z_0} \\ &= j \left(\frac{f_n l}{l^2 + f_n^2 Q^2} - \frac{1 - f_n^2}{f_n} \right) + \frac{f_n^2 Q}{l^2 + f_n^2 Q^2}. \quad (3) \end{aligned}$$

A second resonant frequency corresponds to the conditions of no load, or the secondary winding(s) being open can be found. It is defined as

$$f_{r2} = \frac{1}{2\pi\sqrt{(L_r + L_m)C_r}} = f_{r1} \sqrt{\frac{l}{1+l}}. \quad (4)$$

From (2), we can see that the voltage conversion ratio of an LLC converter is not only related to f_s but also related to the load situation and the inductance ratio. A family of plots of the voltage gain versus normalized frequency for different values of Q , with $l = 0.2$ is shown in Fig. 6. It is visible that a load-independent operation with unity gain happens at the resonance frequency f_{r1} , where all the curves are tangent. Step-up operation is available below the resonance frequency, whereas buck mode operates above the resonance frequency. Moreover, a shrinking effect [17] of increasing l values can be observed by plotting voltage gain curve for different values of l with $Q = 0.7$ in Fig. 7, which implies that a higher l value leads to a higher voltage gain within a smaller frequency range at the cost of increasing the circulating current due to smaller input impedance.

Soft-switching is the most desirable advantage of a resonant converter due to its capability to reduce switching loss and EMI. The LLC topology possesses the soft-switching feature as the ZVS for input inverting choppers and the ZCS for output rectifiers [30], which minimizes the switching losses of the MOSFET-based inverter. However, FHA provides only a necessary condition for ZVS operation of the primary switches but does not guarantee the secondary rectifiers to work in ZCS [17]. For the primary side, ZVS occurs when the input impedance of the resonant tank is inductive, whereas ZCS occurs when

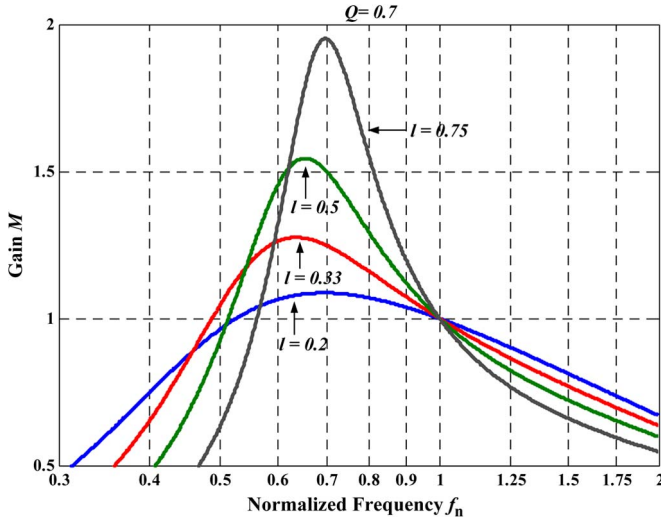


Fig. 7. Shrinking effect of increasing the inductance ratio.

the input impedance is capacitive. From (3), we can tell that the imaginary part of the normalized impedance Z_n is always positive when $f_n \geq 1$, which promised inductive mode above the resonance. For $f_n < 1$, the borderline condition between capacitive and inductive mode can be found by imposing that the imaginary part of (3) is zero [17]. The analytical results are the following:

$$f_{nZ}(l, Q) = \sqrt{\frac{Q^2 - l(1+l) + \sqrt{[Q^2 - l(1+l)]^2 + 4Q^2l^2}}{2Q^2}} \quad (5)$$

$$Q_Z(f_n, l) = \sqrt{\frac{l}{1-f_n^2} - \left(\frac{l}{f_n}\right)^2} \quad (6)$$

where the normalized frequency should be limited by $\sqrt{l/(1+l)} < f_n < 1$ for (6) to be true.

By substituting (6) into (2), the critical voltage gain available in the ZVS condition can be expressed by

$$M_Z(f_n, l) = \frac{f_n}{\sqrt{f_n^2(1+l) - l}} \quad (7)$$

Moreover, by letting $Q = 0$, the no-load voltage gain can be obtained as follows:

$$M_{NL}(f_n, l) = \frac{1}{\left|1 + l - \frac{l}{f_n^2}\right|} \quad (8)$$

According to (7) and (8), the boundary between capacitive and inductive mode in the region between the two resonant frequencies (below-resonance operating region) and the no-load gain are both shown in Fig. 6 with $l = 0.2$.

Achieving the primary-side ZVS operation from full load to zero load is the most important target in selecting the resonant tank circuit parameters. To attain this purpose, some general design guidelines for different types of applications can be concluded based on the earlier analysis. For constant output voltage with various load applications, there is no better choice

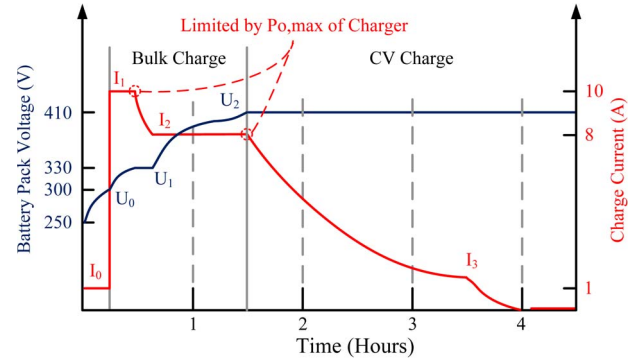


Fig. 8. Charging profile of a 410-V lithium-ion battery pack.

than designing the converter to operate at resonant frequency when the input is at nominal value since this load-independent point occurs in the ZVS region. As for widely adjustable output with variable resistive load, there are two design choices. First, the maximum output voltage with full-load occurs in region 2 (below resonance region), as shown in Fig. 6. This is the preferable operation mode of an LLC converter according to operation mode analysis [19], [21], [31] because primary ZVS and secondary ZCS operations can be realized at the same time as long as the operation point does not go across the borderline of capacitive mode and inductive mode in Fig. 6. However, it is also harder to obtain an optimum design because the FHA model is not very accurate in this region, and no closed-form solution can be found in the exact model. Second, the full-load operation occurs in region 1 (above resonance region) while the boost capability of the resonant tank is left to handle the minimum input during mains dips. This mode is easier to handle since the input impedance is always inductive, and the errors caused by the FHA approach are minor in this region [32]. However, the ZCS operation of the secondary rectifier only appears in light-load conditions [14], [19].

Moreover, no matter which mode has been targeted, the common issue for optimization is achieving required voltage gain in the worst-case scenario while minimizing the circulating reactive energy, which is a necessary condition to ensure soft-switching operation and to reduce conduction losses.

Applications adopting the aforementioned LLC topology have been discussed in a number of publications and application notes in the industry. However, these analyses do not cover wide-adjustable-range output voltage with lithium-ion battery load applications; therefore, the impacts of the charging profile on design considerations need to be investigated.

III. IMPACTS OF BATTERY LOAD PROPERTY ON THE DESIGN CONSIDERATIONS OF LLC CONVERTERS

As in Section I, the charge rate of a lithium-ion battery charger should be controlled according to the charging profile and the battery condition. A typical charging profile of a 400-V battery pack is shown in Fig. 8. Similar to Fig. 3, a trickle charge stage with a CC of 0.1 C.¹ I_0 is performed when

¹C-rate is referred to the charge rate of a battery in terms of its rated capacity. For example, if a battery is rated at 20 Ah, 1 C means the battery is charged at a current of 20 A, and 0.1 C means charging the battery at 2 A.

the battery is deeply depleted. A bulk charge follows after the voltage has risen above the trickle charge threshold. A full-rate charge may not be able to be maintained during the whole bulk-charge stage due to limitations of the maximum output power of the charger. Moreover, the charging actions may be modified as a response to the battery condition variation. Therefore, different CC (in the range of 0.2–1 C) charge stages may exist in the bulk-charge stage [33]. After the CC charge ends, the CV stage begins when the battery voltage reaches a certain value. Furthermore, all the preset charging currents (I_0, I_1, I_2) and threshold voltages (U_0, U_1, U_2) should be able to be modified by users to match different battery packages. Therefore, it is particularly important for an LLC-converter-based lithium-ion battery charger to realize current or voltage regulation in any point of the highlighted area marked as “working region” in Fig. 6 as the operating conditions and load vary widely [24].

From a designer’s point of view, the key is to incorporate the design constraints related to achieving soft-switching under all operating conditions and zero-load operation capability. Therefore, the worst-case scenario in different operation modes with a battery load should be identified to get the constraints.

A. Full-Load Operation in Boost Mode ($M > 1$)

It is intuitive that, for a resistive load in the boost mode, the worst-case scenario occurs when the output voltage is regulated at its maximum value, and the input voltage drops to its minimum under a full-load condition. However, for the charger applications, the load characteristic varies nonlinearly during the whole charge process depending on the charging profile. It is not so easy to identify the worst-case operation point.

Unlike a resistive load, the quality factor Q and the required conversion gain M are coupled according to the charging profile. For example, as shown in Fig. 8, the output power of the charger hits the limitation twice during the bulk-charge stage. It is hard to see directly which operation point is closer to the edge of the inductive region because Q and M vary in reverse direction and affect the characteristic inversely.

On the other hand, all kinds of charging profiles are needed for different battery packs, but all the profiles should be compromised with the maximum output power of the converter. Therefore, maintaining the maximum power output during the whole charge process at minimal input voltage is reasonable to be seen as the overall heaviest load for the charger, although it may not be practical due to safety and cycle life consideration [34].

In short, the target is to distinguish the worst-case scenario for achieving soft-switching from the constant maximum power (CMP) charging profile. Under the circumstances, the quality factor and the required conversion gain are related by the following equation, which can be obtained according to the definition of these two parameters in Section II:

$$Q_{\text{CMP}}(Z_0, M) = \frac{\pi^2}{8} \frac{P_{\text{out,max}}}{(M V_{\text{in,min}})^2} Z_0. \quad (9)$$

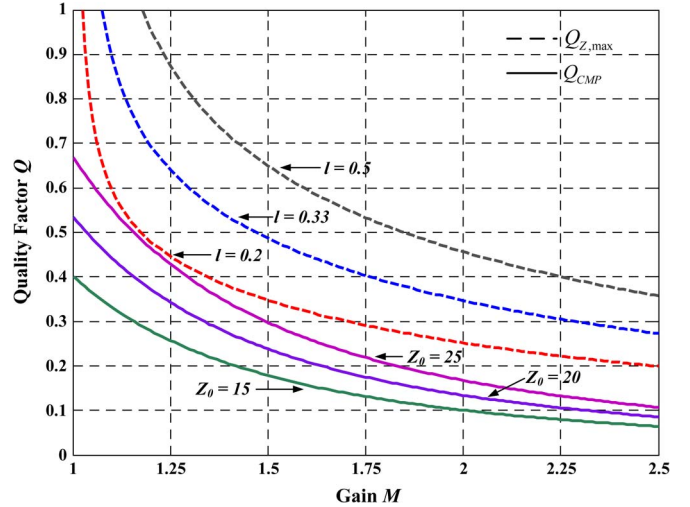


Fig. 9. Operation trajectories of CMP charge and ZVS boundaries for different Z_0 and l values.

On the other hand, the maximum quality factor $Q_{Z,\text{max}}$ that allows the required voltage gain at the boundary between capacitive and inductive modes can be obtained by solving for f_n in (7) and then substituting into (6), resulting into

$$Q_{Z,\text{max}}(l, M) = \frac{l}{M} \sqrt{\frac{1}{l} + \frac{M^2}{M^2 - 1}}. \quad (10)$$

The variation of the quality factor during the constant power charge is implied in (9), whereas the limitation for achieving primary-side ZVS is indicated in (10). It is clear that the operating trajectory mainly depends on the characteristic impedance Z_0 , and the ZVS boundary relies on the inductance ratio l . A few operating trajectories (solid line) and boundaries (dash line) are shown by the swap voltage gain and the quality factor for different values of Z_0 and l in Fig. 9.

A lifting effect of increasing the l value can be observed in boundary curves, which means a higher inductance ratio brings higher capability for the same required voltage gain. The price for higher capability is a higher circulating current in the resonant tank because of relatively smaller magnetizing inductance. The lifting effect is consistent with the shrinking effect, as previously mentioned in Section II, because it is actually the same phenomenon presented from different views. In addition, the vertical asymptote of $Q_{Z,\text{max}}$ is $M = 1$, which again illustrates that the unity gain is the load-independent point.

On the other hand, the operating trajectories are pushed toward the boundaries by increasing the characteristic impedance Z_0 . The motivation is to reduce the circulating current.

Thus, the intent to reduce the circulating reactive energy for minimizing the conduction losses during the optimal design procedure will eventually make the operating trajectory to touch the boundary at a certain point, and this touching point is actually the worst-case operation point in boost mode that we are trying to identify. This condition can be mathematically described by

$$\begin{cases} Q_{Z,\text{max}}(l, M) - Q_{\text{CMP}}(Z_0, M) = 0 \\ \frac{\partial(Q_{Z,\text{max}}(l, M) - Q_{\text{CMP}}(Z_0, M))}{\partial M} = 0. \end{cases} \quad (11)$$

Substituting (9) and (10) into (11), we have

$$\begin{cases} \frac{l}{M} \sqrt{\frac{1}{l} + \frac{M^2}{M^2-1}} - \frac{\pi^2 Z_0 P_{out,max}}{8 M^2 V_{in,min}^2} = 0 \\ -\frac{l \sqrt{\frac{1}{l} + \frac{M^2}{M^2-1}}}{M^2} + \frac{1}{2} \frac{l \left(\frac{2M}{M^2-1} - \frac{2M^3}{(M^2-1)^2} \right)}{M \sqrt{\frac{1}{l} + \frac{M^2}{M^2-1}}} + \frac{1}{4} \frac{\pi^2 Z_0 P_{out,max}}{M^3 V_{in,min}^2} = 0. \end{cases} \quad (12)$$

The analytical results can be found as follows:

$$\begin{cases} M_{crit} = \sqrt{1 + \sqrt{\frac{l}{1+l}}} \\ Z_{0,max} = \frac{8}{\pi^2} \frac{V_{in,min}^2}{P_{out,max}} \left(\sqrt{l(1+l)} + l \right). \end{cases} \quad (13)$$

The results indicate that, during the CMP charging process, the LLC resonant converter is running at the boundary of capacitive and inductive modes (the critical operating point) when the characteristic impedance is designed to be the allowed maximal value $Z_{0,max}$ and the required voltage gain equals the critical value M_{crit} . Both $Z_{0,max}$ and M_{crit} are related to design parameter l .

In conclusion, the worst case for primary-side ZVS operation in boost mode is found using charging profile specifications and FHA-based analysis of boundaries between capacitive and inductive modes. Many traditional design procedures can be used by seeing the worst-case operation point found here as the full-load operation point.

B. Zero-Load Operation in Buck Mode ($M < 1$)

Zero-load operation occurs when the voltage developed across L_m and reflected to the secondary side is lower than the battery voltage so that the output rectifiers cannot be conducted over an entire switching cycle. There is no difference from an infinite resistive load since the battery has been cut off from the resonant tank circuit. The design issues related to this mode are presented in the following.

IV. DESIGN CONSTRAINTS

The most important object in designing the LLC converter is to achieve soft-switching operation in the whole working range. To attain this purpose, design constraints in different modes are discussed respectively.

A. Zero-Load ZVS Operation Capability in Buck Mode

The worst-case scenario for ZVS operation in buck mode occurs when the output voltage is regulated at its minimum value, and the maximum input voltage is applied to the converter under the no-load condition [35]. In this case, the switching frequency is adjusted to its maximum value to step down the input voltage. The zero-load operation, regarded as cutoff mode, has been discussed in [14]. The normalized cutoff frequency at minimum conversion gain can be expressed as

$$f_{nco} = \frac{\pi}{2} \sqrt{\frac{l}{1+l}} \frac{1}{\cos^{-1} \left[\frac{1}{M_{min}(1+l)} \right]} \quad (14)$$

with the minimum voltage conversion defined as

$$M_{min} = \frac{nV_{out,min}}{V_{in,max}} \quad (15)$$

and the normalized cutoff frequency defined as

$$f_{nco} = \frac{f_{co}}{f_{r1}}. \quad (16)$$

Mathematically, a necessary condition for the cutoff frequency to exist is

$$M_{min} \geq \frac{1}{1+l}. \quad (17)$$

Moreover, (14) can be rewritten as

$$\frac{1}{M_{min}(1+l)} = \cos \left(\frac{\pi}{2} \sqrt{\frac{l}{1+l}} \frac{1}{f_{nco}} \right). \quad (18)$$

Expanding the cosine function in MacLaurin series to the second order and assigning value for $f_{nco} = f_{nmax} = (f_{smax}/f_{r1})$, the resulting equation can be solved for l [22] is

$$l = \left(\frac{1}{M_{min}} - 1 \right) \frac{8f_{nmax}^2}{8f_{nmax}^2 - \pi^2}. \quad (19)$$

To be noted, the junction capacitance of the rectifier diode has not been taken into account in the given analysis. Therefore, the maximum switching frequency should be limited to 1.5–2.5 times the resonant frequency to avoid the effect of this parasitic parameter at a higher frequency range [6], [36].

The peak value of the tank current in cutoff mode is also provided [14] as follows:

$$I_{mco} = \frac{V_{in,max}}{2\pi f_{r1} L_{m0}} \sqrt{\left(1 + \frac{1}{l}\right) M_{min}^2 - \frac{1}{l(1+l)}}. \quad (20)$$

In order to guarantee ZVS in this mode, the current I_{mco} must be large enough to discharge the MOSFETs junction capacitors within the dead time, which can be represented by [12]

$$I_{mco} \geq \frac{4C_{oss} V_{in,max}}{t_d} \quad (21)$$

where $V_{in,max}$ is the maximum input voltage, C_{oss} is the MOSFET junction capacitance, and t_d is the dead time.

Substituting (20) into (21) and solving for L_{m0} yields

$$L_{m0} \leq \frac{t_d}{8\pi f_{r1} C_{oss}} \sqrt{\left(1 + \frac{1}{l}\right) M_{min}^2 - \frac{1}{l(1+l)}}. \quad (22)$$

B. Full-Load ZVS Operation Capability in Boost Mode

The worst-case operating point has been recognized from the CMP charging profile in Section III. The full-load ZVS operation can be promised globally in the boost mode as long as the worst case is designed properly.

As previously mentioned, there is a preferable operation mode featured with primary ZVS and secondary ZCS capability in the boost-mode operation, which is referred to as DCMB2

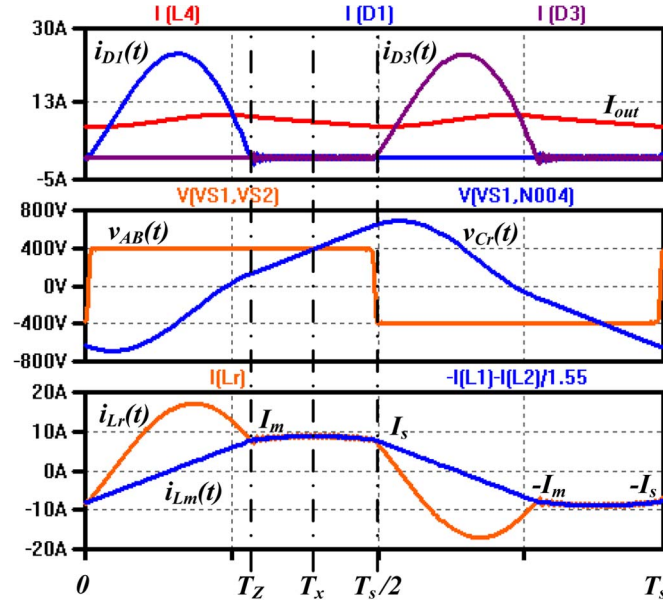


Fig. 10. Simulation waveforms of the LLC resonant full bridge operated in DCMB2 mode.

mode in [14] and [21] or PO mode in [19]. However, this mode is complicated by nonlinear equation solving. To avoid the complexity, a special operating point characterized by a nearly flat tank current during the interval of multiresonance in this mode is targeted [22]. The simulation waveforms of this operating point are shown in Fig. 10.

As shown in Fig. 10, in the interval $(T_Z, T_s/2)$, when the magnetizing inductor joins the resonance, the tank current looks flat. Therefore, it is reasonable to assume

$$i_{Lr}(T_Z) = i_{Lm}(T_Z) = I_m = i_{Lr}(T_s/2) = i_{Lm}(T_s/2) = I_s. \quad (23)$$

This equality holds true if the peak of the multiresonant current occurs exactly at the midpoint T_x of the interval $(T_Z, T_s/2)$ [22], i.e.,

$$T_x = \frac{1}{2} \left(T_Z + \frac{T_s}{2} \right). \quad (24)$$

Moreover, for this to occur, the voltage across the resonant capacitor at this moment must equal the minimal input voltage for the worst case, i.e.,

$$V_{Cr}(T_x) = V_{in,min}. \quad (25)$$

Based on assumption (23) and the symmetry of tank current, we have

$$-i_{Lr}(0) = i_{Lr}(T_s/2) = i_{Lr}(T_Z) = I_s. \quad (26)$$

Because during the interval $(0, T_Z)$, the converter actually works as a series resonant converter, and the tank current is expressed by a sine function with series resonant period T_{r1} . Therefore, (26) implies

$$T_Z = \frac{1}{2} T_{r1} = \frac{1}{2f_{r1}}. \quad (27)$$

With all the given characteristics, a required magnetizing inductance $T_Z = (1/2)T_{r1} = (1/2f_{r1})$ may be found and ex-

pressed by other design parameters and the critical operating conditions (see Appendix)

$$L_m = \frac{n^2}{f_{r1}} \frac{V_{out,crit}}{4nI_{in,crit} + (\pi^2 l M_{crit} - 4)I_{out,crit}}. \quad (28)$$

According to the discussion above, the maximum value of magnetizing inductance is limited by inequality (22) to guarantee no-load ZVS operation in buck mode, while (28) provides the value of the magnetizing inductor that makes the converter operate in the desired DCMB2 boost mode and ensures the worst-case full-load ZVS operation capability. Therefore, if the value resulting from (28) fulfills (22), soft-switching is ensured throughout the whole operating range [22].

V. DESIGN PROCEDURE

The proposed design procedure for the PHEV battery charger application based on the analysis presented earlier can be outlined in eight steps, starting from the design specification detailed in Table I.

Step 1) Select transformer turns ratio n . The minimal transformer turns ratio should be selected at unity gain when the input voltage and the output voltage are both at a minimum value, i.e.,

$$n = \frac{V_{in,min}}{V_{out,min}}. \quad (29)$$

In this case, the converter operates at a load-independent point that ensures full-load operation capability at minimal input voltage. The step-down operation can be implemented to regulate the output when the input is back to the nominal level or goes to the maximum. The step-up mode is targeted when the output voltage rises.

Step 2) To make sure the output is always under regulation, the minimum dc voltage gain M_{min} should be calculated by using (15).

Step 3) Calculate inductance ratio l by (19). The results from Steps 2 and 3 ensure that the converter enters the cutoff mode at minimum output and maximum input when the switching frequency is regulated to the maximum value.

Step 4) Use (13) to calculate the worst-case conversion gain M_{crit} and the maximum characteristic impedance $Z_{0,max}$. Then, calculate the other critical operating condition

$$I_{out,crit} = \frac{P_{out,max}}{V_{out,crit}} = \frac{P_{out,max}}{M_{crit} V_{in,min}/n} \quad (30)$$

$$I_{in,crit} = \frac{P_{out,max}}{\eta V_{in,min}}. \quad (31)$$

Step 5) Calculate the magnetizing inductance L_m required for operating in DCMB2 mode at a critical point using (28).

Step 6) Check that the value of L_m fulfills the no-load ZVS condition (22). If not, try either reducing the

TABLE I
DESIGN SPECIFICATION FOR THE LLC RESONANT CONVERTER

Parameter	Designator	Value
Input Voltage Range	$V_{in,min} \sim V_{in,max}$	390 – 420 [V]
Input Voltage Nominal	$V_{in,nom}$	400 [V]
Output Voltage Range	$V_{out,min} \sim V_{out,max}$	250 – 450 [V]
Maximum Output Power	$P_{out,max}$	3.3 [kW]
Resonant Frequency	f_{r1}	150 [kHz]
Maximum Operating Frequency	$f_{s,max}$	220 [kHz]
Expected Efficiency	η	98 [%]

maximum operating frequency $f_{s,max}$ or increasing resonant frequency f_{r1} or else increasing dead time t_d and go back to Step 2. In addition, adjust one or more of the above parameters also if L_m is much lower than the minimum needed for ZVS [22].

Step 7) Calculate the value of resonant capacitor C_r and resonant inductance L_r by (17A) and (18A). Then, check that the value of Z_0 is smaller than the allowed maximum value of $Z_{0,max}$. If not, try either reducing the maximum operating frequency $f_{s,max}$ or increasing resonant frequency f_{r1} slightly and go back to Step 2.

Step 8) Calculating the minimum operating frequency $f_{s,min}$. The switching current at maximum conversion gain $I_{s,max}$ can be obtained by assigning value for $V_{out} = V_{out,max}$ in (20A). The other maximum output voltage operating conditions can be calculated according to (30) and (31). Finally, the minimum operating frequency can be calculated by (8A).

VI. EXPERIMENTAL RESULTS

A prototype of the full-bridge LLC resonant converter has been built to verify the theoretical analysis, which is based on the specification given in Table I. The key parameters resulting from the proposed design procedure are given in Table II, where the actual measured values are also shown. It is noted that the magnetic integration is adopted to make the system more compact [28]. The primary and secondary windings are distributed in two asymmetrical separate slots of the core bobbin to form the relatively large leakage inductance. The circuit components used in the prototype converter are provided in Table III.

To verify the whole range ZVS capability, the FHA-based characteristic of the designed LLC tank has been plotted versus normalized frequency f_n and quality factor Q in Fig. 11. The borderline between the capacitive mode and the inductive mode, and the CMP charging profile are also shown in Fig. 11. As shown in this figure, the CMP operating trajectory keeps a reasonable safe distance from the ZVS/ZCS boundary, which confirms the soft-switching operation for the whole operation range.

The performance of the CMP charge is tested. An electronic load is used to simulate the load characteristics of the lithium-

TABLE II
RESONANT TANK PARAMETER DESIGN RESULTS

Parameter (Designator)	Calculated Value	Measured Value
Inductance Ratio (l)	0.197	0.19
Critical Voltage Gain (M_{crit})	1.186	1.183
Maximum Characteristic Impedance ($Z_{o,max}$)	25.52 [Ω]	24.86 [Ω]
Characteristic Impedance (Z_0)	25.51 [Ω]	24.85 [Ω]
Magnetizing Inductance (L_m)	133.10 [μ H]	141.10 [μ H]
Series Resonant Inductance (L_r)	26.25 [μ H]	26.50 [μ H]
Series Resonant Capacitor (C_r)	40.33 [nF]	42.90 [nF]
Transformer Turns ratio (n)	1.56	1.57
Series Resonant Frequency (f_{r1})	154.70 [kHz]	149.30 [kHz]
Minimum Switching Frequency ($f_{s,min}$)	83.33 [kHz]	81.69 [kHz]

TABLE III
COMPONENTS USED IN THE PROTOTYPE CONVERTER

Component	Manufacturer	Part #
MOSFET	Infineon Technologies	IPW60R041C6
Diode Rectifiers	Fairchild Semiconductor	FFH60UP60S
Resonant Film Capacitors	EPCOS	MKP 13×3.3 [nF]
Magnetic Ferrite core of Transformer	Magnetics	0R48020EC
Litz-wire	HM Wire International	AWG38×400
Output Film Capacitors	Vishay	MMKP383 6×1[μ F]

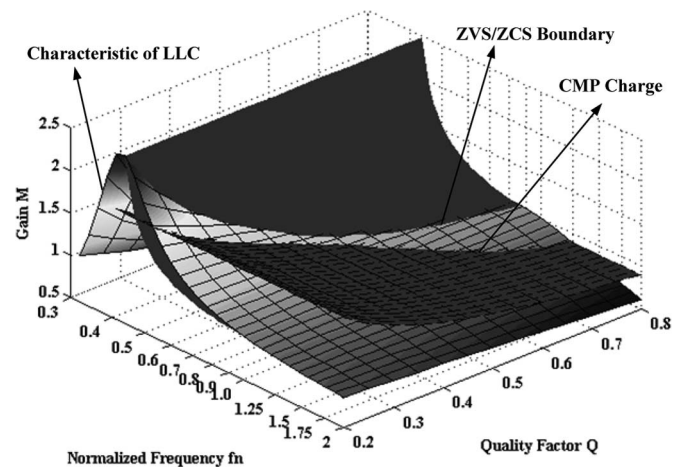


Fig. 11. Verification of a design result by FHA analysis.

ion battery pack in the experiments. Experimental waveforms of the voltage across resonant tank v_{AB} , voltage across resonant capacitor v_{Cr} , resonant tank current i_{Lr} , and magnetizing current i_{Lm} are shown in Fig. 12 at $V_{in} = 390$ V and $P_{out} = P_{out,max} = 3.3$ kW. In this figure, the capability for primary-side ZVS turn-on is noted since the resonant tank current lags

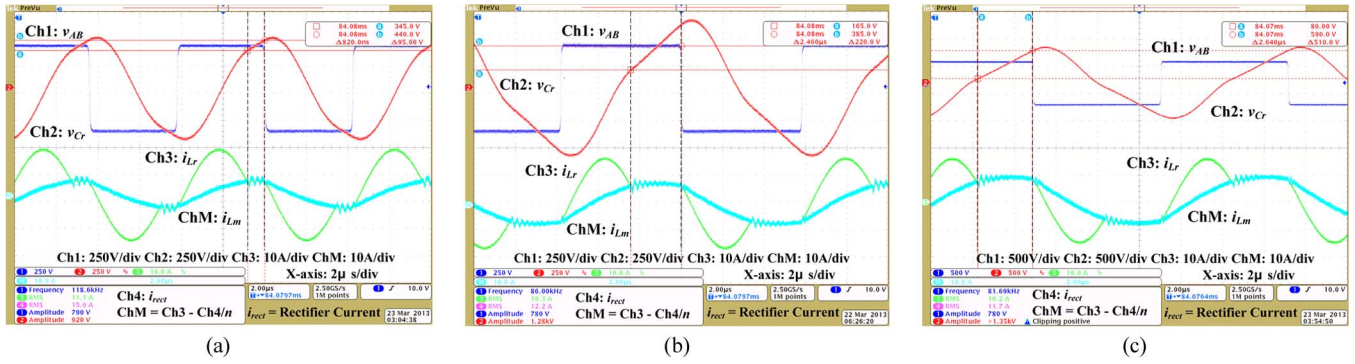


Fig. 12. Experimental waveforms. (a) CMP charge at $V_{out} = 300$ V, $I_{out} = 11$ A, and $f_s = 118.6$ kHz. (b) CMP charge at $V_{out} = 410$ V, $I_{out} = 8$ A, and $f_s = 86$ kHz. (c) CMP charge at $V_{out} = 450$ V, $I_{out} = 7.3$ A, and $f_s = 81.69$ kHz.

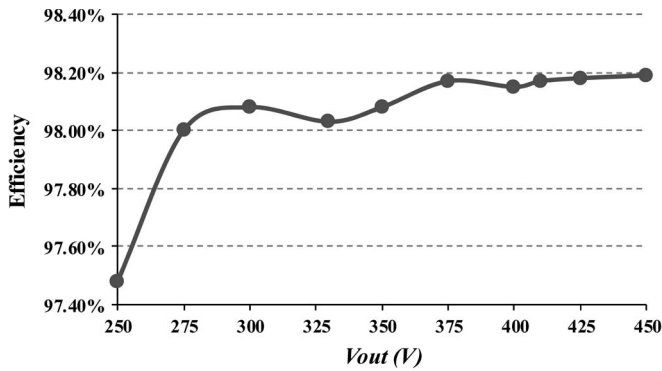


Fig. 13. Measured efficiency versus output voltage at $P_o = 3.3$ kW and $V_{in} = 390$ V.

the voltage across the resonant tank. It is also proven that the desired DCMB2 mode operation is ensured for a wide output range because the features of these waveforms match the desired features discussed in Section IV. The efficiency of the converter as a function of output voltage for the CMP charge is shown in Fig. 13. It is observed that the efficiency increases with the output voltage and achieves 98.2% at $V_{out} = 450$ V. In addition, the charging profile shown in Fig. 8 is implemented in the prototype. The efficiency curve of the bulk-charge stage is provided in Fig. 14. It is shown that the efficiency is higher than 98% during the whole bulk-charge stage. Finally, the efficiency curves of the CV charge stage at outputs of 250 and 410 V are given in Figs. 15 and 16, respectively. The conversion performance at light load condition can be evaluated according to these two curves. It can be seen that the efficiency is mostly above 95.5% during the CV charge stage. The light load efficiency is about 90.5% when the charge current drops to 0.1 C.

VII. CONCLUSION

This paper analyzed the wide-adjustable-range LLC resonant converter applied in lithium-ion battery charger systems and proposed a step-by-step design methodology. The different design requirements for resistive load and battery load are investigated based on the FHA approach. Considering the charging profiles, the worst-case scenarios for the primary-side ZVS operation under full-load and no-load conditions are identified, respectively. Then, the design constraints for achieving soft-switching operation under all working conditions are

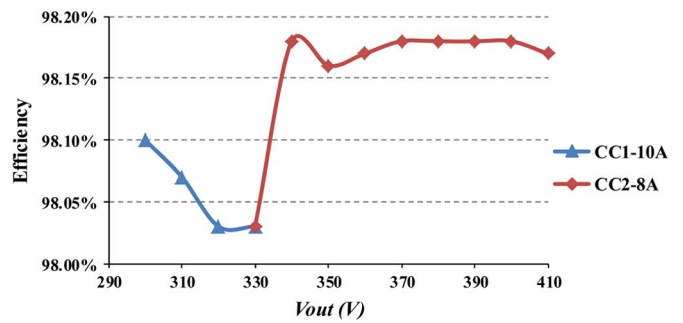


Fig. 14. Measured efficiency versus output voltage of multiple CC charge stage. CC1 stage: $I_o = 10$ A and $V_o = 300 \sim 330$ V. CC2 stage: $I_o = 8$ A and $V_o = 330 \sim 410$ V.

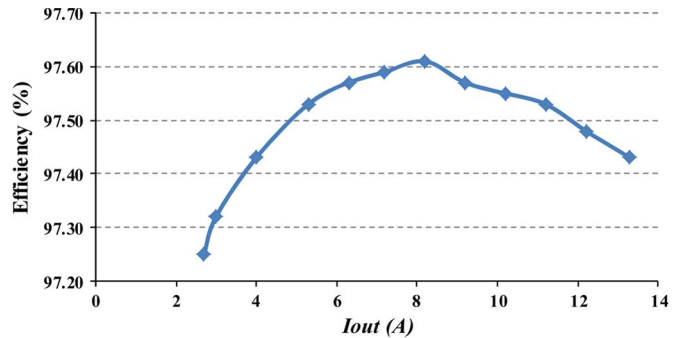


Fig. 15. Measured efficiency versus output current at $V_o = 250$ V and $V_{in} = 390$ V.

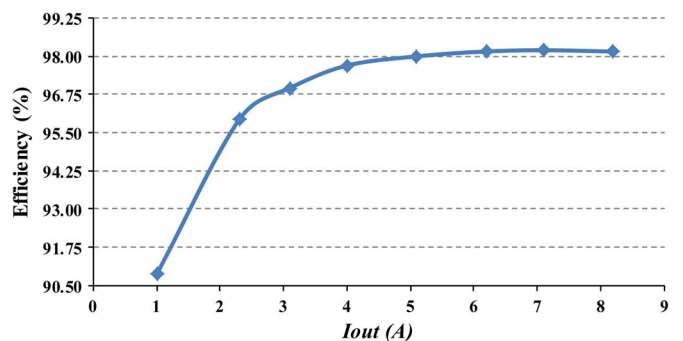


Fig. 16. Measured efficiency versus output current at $V_o = 410$ V and $V_{in} = 390$ V.

analytically derived based on specific operating mode analysis. Finally, all the discussion has led to the design procedure that ensures soft-switching under all operating conditions, and the

preferable boost operation mode under full load conditions. A 3.3-kW 400-V-input 250–450-V-output LLC converter is built using the proposed method, which achieves 98.2% peak efficiency.

APPENDIX
MODEL ANALYSIS OF DCMB2 OPERATION IN
BOOST-MODE OPERATION

In a half switching period, the operation model of the LLC converter presented in Section IV-B can be approximately described by the following equations.

The resonant tank current is

$$\begin{cases} i_{Lr}(t) = \frac{I_s}{\sin\theta_1} \sin(2\pi f_{r1}t - \theta_1), & 0 \leq t \leq \frac{T_{r1}}{2} \\ i_{Lr}(t) = I_s, & \frac{T_{r1}}{2} \leq t \leq \frac{T_s}{2}. \end{cases} \quad (1A)$$

The magnetizing current is

$$\begin{cases} i_{Lm}(t) = I_s(4f_{r1}t - 1), & 0 \leq t \leq \frac{T_{r1}}{2} \\ i_{Lm}(t) = I_s, & \frac{T_{r1}}{2} \leq t \leq \frac{T_s}{2}. \end{cases} \quad (2A)$$

The voltage across the resonant capacitor is

$$\begin{cases} v_{Cr}(t) = v_{Cr}(0) + \frac{1}{C_r} \int_0^t i_{Lr}(t)dt, & 0 \leq t \leq \frac{T_{r1}}{2} \\ v_{Cr}(t) = v_{Cr}\left(\frac{T_{r1}}{2}\right) + \frac{I_s}{C_r} \left(t - \frac{T_{r1}}{2}\right), & \frac{T_{r1}}{2} \leq t \leq \frac{T_s}{2}. \end{cases} \quad (3A)$$

The secondary current, flowing through rectifier D_1 is

$$i_{D1}(t) = n [i_{Lr}(t) - i_{Lm}(t)]. \quad (4A)$$

It is now necessary to relate the unknown quantities in (1A), (2A), θ_1 , I_s , and f_s to the operating conditions $V_{in,min}$, I_{in} , and I_{out} .

The converter's dc output current is

$$I_{out} = \frac{2}{T_s} \int_0^{T_{r1}/2} i_{D1}(t)dt. \quad (5A)$$

Substituting (4A) in (5A), taking (1A) and (2A) into consideration and developing the integral, we have

$$I_{out} = \frac{2nI_s}{\pi \tan\theta_1} \frac{T_{r1}}{T_s}. \quad (6A)$$

The converter's dc input current is expressed as

$$I_{in} = \frac{2}{T_s} \int_0^{T_s/2} i_{Lr}(t)dt = I_s \left[\left(\frac{2}{\pi \tan\theta_1} - 1 \right) \frac{T_{r1}}{T_s} + 1 \right]. \quad (7A)$$

The simultaneous solution of (6A) and (7A) provides

$$f_s = \left(1 - \frac{nI_{in} - I_{out}}{nI_s} \right) f_{r1} \quad (8A)$$

$$\tan\theta_1 = \frac{2}{\pi} \left(1 - n \frac{I_{in} - I_s}{I_{out}} \right). \quad (9A)$$

The value of $v_{Cr}(T_s/2)$ is given by

$$v_{Cr}\left(\frac{T_s}{2}\right) = v_{Cr}(0) + \frac{1}{C_r} \int_0^{T_s/2} i_{Lr}(t)dt = v_{Cr}(0) + \frac{I_{in}T_s}{2C_r}. \quad (10A)$$

By symmetry, we have

$$v_{Cr}\left(\frac{T_s}{2}\right) = -v_{Cr}(0). \quad (11A)$$

Substituting (11A) in (10A), we find

$$v_{Cr}(0) = -\frac{T_s I_{in}}{4C_r}. \quad (12A)$$

By substituting (12A) in (3A), it is possible to find

$$v_{Cr}\left(\frac{T_{r1}}{2}\right) = \frac{I_s}{C_r} \left(\frac{T_{r1}}{2\pi \tan\theta_1} + \frac{T_{r1} - T_s}{4} \right). \quad (13A)$$

Considering (27), (24) can be rewritten

$$T_x = \frac{1}{4}(T_{r1} + T_s). \quad (14A)$$

By combining (3A), (13A), and (14A), the expression of $v_{Cr}(T_x)$ becomes

$$v_{Cr}(T_x) = \frac{I_s}{C_r} \frac{T_{r1}}{2\pi \tan\theta_1}. \quad (15A)$$

Substituting (25) and (9A) in (15A) and solving for I_s

$$I_s = \frac{4C_r V_{in,min}(I_{out} - nI_{in})}{T_{r1}I_{out} - 4nC_r V_{in,min}}. \quad (16A)$$

From the definition of inductance ratio and resonant frequency, we have

$$L_r = lL_m \quad (17A)$$

$$C_r = \frac{1}{L_r(2\pi f_{r1})^2} = \frac{1}{lL_m(2\pi f_{r1})^2}. \quad (18A)$$

By substituting (18A) into (16A), I_s can be rewritten as

$$I_s = \frac{V_{in,min}(I_{out} - nI_{in})}{\pi^2 l L_m f_{r1} I_{out} - nV_{in,min}}. \quad (19A)$$

Note that, in the interval $(0, T_Z)$, when the secondary rectifiers are conducting, the magnetizing inductor is clamped by the output voltage; therefore, the switching current I_s can be also expressed by

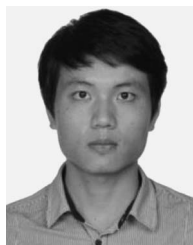
$$I_s = I_m = \frac{nV_{out}}{4L_m f_{r1}}. \quad (20A)$$

Finally, solving for L_m from (19A) and (20A) and introducing the critical voltage gain discussed in Section III, a constraint may be found on the magnetizing inductance for the converter operating in this targeted mode

$$L_m = \frac{n^2}{f_{r1}} \frac{V_{out,crit}}{4nI_{in,crit} + (\pi^2 l M_{crit} - 4)I_{out,crit}}. \quad (21A)$$

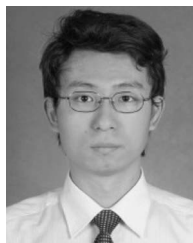
REFERENCES

- [1] C. Mi, M. A. Masrur, and D. W. Gao, *Hybrid Electric Vehicles: Principles and Applications with Practical Perspectives*. Hoboken, NJ, USA: Wiley, 2011.
- [2] X. Zhang and C. Mi, *Vehicle Power Management: Modeling, Control and Optimization*. Berlin, Germany: Springer-Verlag, 2011.
- [3] Z. Menyng, Y. Yan, and C. C. Mi, "Analytical approach for the power management of blended-mode plug-in hybrid electric vehicles," *IEEE Trans. Veh. Technol.*, vol. 61, no. 4, pp. 1554–1566, May 2012.
- [4] Z. Bingzhan, C. C. Mi, and Z. Mengyang, "Charge-depleting control strategies and fuel optimization of blended-mode plug-in hybrid electric vehicles," *IEEE Trans. Veh. Technol.*, vol. 60, no. 4, pp. 1516–1525, May 2011.
- [5] M. Yilmaz and P. T. Krein, "Review of battery charger topologies, charging power levels, and infrastructure for plug-in electric and hybrid vehicles," *IEEE Trans. Power Electron.*, vol. 28, no. 5, pp. 2151–2169, May 2013.
- [6] F. Musavi, M. Craciun, M. Edington, W. Eberle, and W. G. Dunford, "Practical design considerations for a LLC multi-resonant DC-DC converter in battery charging applications," in *Proc. 27th Annu IEEE APEC Expo.*, 2012, pp. 2596–2602.
- [7] D. Gautam, F. Musavi, M. Edington, W. Eberle, and W. G. Dunford, "An automotive on-board 3.3 kW battery charger for PHEV application," in *Proc. IEEE VPPC*, 2011, pp. 1–6.
- [8] K. Keun-Wan, K. Dong-Hee, W. Dong-Gyun, and L. Byoung-Kuk, "Topology comparison for 6.6 kW On board charger: Performance, efficiency, and selection guideline," in *Proc. IEEE VPPC*, 2012, pp. 1520–1524.
- [9] A. Khaligh and S. Dusmez, "Comprehensive topological analysis of conductive and inductive charging solutions for plug-in electric vehicles," *IEEE Trans. Veh. Technol.*, vol. 61, no. 8, pp. 3475–3489, Oct. 2012.
- [10] H. Bai and C. Mi, "Comparison and evaluation of different DC/DC topologies for plug-in hybrid electric vehicle chargers," *Int. J. Power Electron.*, vol. 4, no. 2, pp. 119–133, Feb. 2012.
- [11] H. Bai, Y. Zhang, C. Semanson, C. Luo, and C. C. Mi, "Modelling, design and optimisation of a battery charger for plug-in hybrid electric vehicles," *IET Elect. Syst. Transp.*, vol. 1, no. 1, pp. 3–10, Mar. 2011.
- [12] L. Bing, L. Wenduo, L. Yan, F. C. Lee, and J. D. van Wyk, "Optimal design methodology for LLC resonant converter," in *Proc. 21st Annu. IEEE APEC Expo.*, 2006, pp. 533–538.
- [13] B. Yang, R. Chen, and F. C. Lee, "Integrated magnetic for LLC resonant converter," in *Proc. 17th Annu. IEEE APEC Expo.*, 2002, vol. 1, pp. 346–351.
- [14] J. F. Lazar and R. Martinelli, "Steady-state analysis of the LLC series resonant converter," in *Proc. 16th Annu. IEEE APEC Expo.*, 2001, vol. 2, pp. 728–735.
- [15] R. L. Steigerwald, "A comparison of half-bridge resonant converter topologies," *IEEE Trans. Power Electron.*, vol. 3, no. 2, pp. 174–182, Apr. 1988.
- [16] T. Duerbaum, "First harmonic approximation including design constraints," in *Proc. 20th INTELEC*, 1998, pp. 321–328.
- [17] S. De Simone, C. Adragna, C. Spini, and G. Gattavari, "Design-oriented steady-state analysis of LLC resonant converters based on FHA," in *Proc. Int. SPEEDAM*, 2006, pp. 200–207.
- [18] R. Beiranvand, B. Rashidian, M. R. Zolghadri, and S. M. H. Alavi, "A design procedure for optimizing the LLC resonant converter as a wide output range voltage source," *IEEE Trans. Power Electron.*, vol. 27, no. 8, pp. 3749–3763, Aug. 2012.
- [19] F. Xiang, H. Haibing, Z. J. Shen, and I. Batarseh, "Operation mode analysis and peak gain approximation of the LLC resonant converter," *IEEE Trans. Power Electron.*, vol. 27, no. 4, pp. 1985–1995, Apr. 2012.
- [20] F. Xiang, H. Haibing, J. Shen, and I. Batarseh, "An optimal design of the LLC resonant converter based on peak gain estimation," in *Proc. 27th Annu. IEEE APEC Expo.*, 2012, pp. 1286–1291.
- [21] R. Yu, G. K. Y. Ho, B. M. H. Pong, B. W. K. Ling, and J. Lam, "Computer-aided design and optimization of high-efficiency LLC series resonant converter," *IEEE Trans. Power Electron.*, vol. 27, no. 7, pp. 3243–3256, Jul. 2012.
- [22] C. Adragna, S. De Simone, and C. Spini, "A design methodology for LLC resonant converters based on inspection of resonant tank currents," in *Proc. 23rd Annu. IEEE APEC Expo.*, 2008, pp. 1361–1367.
- [23] F. Musavi, M. Craciun, D. S. Gautam, W. Eberle, and W. G. Dunford, "An LLC resonant DC-DC converter for wide output voltage range battery charging applications," *IEEE Trans. Power Electron.*, vol. 28, no. 12, pp. 5437–5445, Dec. 2013.
- [24] F. Musavi, M. Craciun, D. Gautam, M. Edington, W. Eberle, and W. G. Dunford, "Control strategies for a LLC multi-resonant DC-DC converter in battery charging applications," in *Proc. 28th Annu. IEEE APEC Expo.*, 2013, pp. 1804–1811.
- [25] R. W. Erickson and D. Maksimovic, *Fundamentals of Power Electronics*, 2nd ed. Secaucus, NJ, USA: Kluwer, 2001.
- [26] X. Rui, H. Hongwen, S. Fengchun, and Z. Kai, "Evaluation on state of charge estimation of batteries with adaptive extended Kalman filter by experiment approach," *IEEE Trans. Veh. Technol.*, vol. 62, no. 1, pp. 108–117, Jan. 2013.
- [27] T. Cleveland and S. Dearborn, "Developing affordable mixed-signal power systems for battery charger Applications," Microchip Technology Inc., Chandler, AZ, USA, Aug. 28, 2006.
- [28] S. De Simone, C. Adragna, and C. Spini, "Design guideline for magnetic integration in LLC resonant converters," in *Proc. Int. SPEEDAM*, 2008, pp. 950–957.
- [29] G. Wei, B. Hua, G. Szatmari-Voicu, A. Taylor, J. Patterson, and J. Kane, "A 10 kW 97%-efficiency LLC resonant DC/DC converter with wide range of output voltage for the battery chargers in plug-in hybrid electric vehicles," in *Proc. IEEE ITEC Expo*, 2012, pp. 1–4.
- [30] C. Wei, R. Ping, and L. Zhengyu, "Snubberless bidirectional DC-DC converter with new CLLC resonant tank featuring minimized switching loss," *IEEE Trans. Ind. Electron.*, vol. 57, no. 9, pp. 3075–3086, Sep. 2010.
- [31] Y. Bo, F. C. Lee, A. J. Zhang, and H. Guisong, "LLC resonant converter for front end DC/DC conversion," in *Proc. 17th Annu. IEEE APEC Expo.*, 2002, vol. 2, pp. 1108–1112.
- [32] R. Beiranvand, B. Rashidian, M. R. Zolghadri, and S. M. H. Alavi, "Using LLC resonant converter for designing wide-range voltage source," *IEEE Trans. Ind. Electron.*, vol. 58, no. 5, pp. 1746–1756, May 2011.
- [33] *User's Manual NLG5*, Brusa Elektronik AG, Sennwald, Switzerland, 2003.
- [34] S. S. Zhang, "The effect of the charging protocol on the cycle life of a Li-ion battery," *J. Power Sources*, vol. 161, no. 2, pp. 1385–1391, Oct. 2006.
- [35] R. Beiranvand, B. Rashidian, M. R. Zolghadri, and S. M. H. Alavi, "Optimizing the normalized dead-time and maximum switching frequency of a wide-adjustable-range LLC resonant converter," *IEEE Trans. Power Electron.*, vol. 26, no. 2, pp. 462–472, Feb. 2011.
- [36] L. Byoung-Hee, K. Moon-Young, K. Chong-Eun, P. Ki-Bum, and M. Gun-Woo, "Analysis of LLC Resonant Converter considering effects of parasitic components," in *Proc. 31st INTELEC*, 2009, pp. 1–6.



Junjun Deng (S'13) received the B.S. and M.S. degrees in electrical engineering from Northwestern Polytechnical University, Xi'an, China, in 2008 and 2011, respectively. He is currently working toward the Ph.D. degree in electrical engineering with Northwestern Polytechnical University and with the University of Michigan, Dearborn, MI, USA (supported by the China Scholarship Council), where he is involved in the modeling and design of ac/dc and dc/dc converters.

His research interests include resonant power conversion and high-performance battery chargers for electric vehicles.



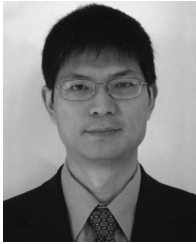
Siqi Li received the B.S. and Ph.D. degrees in electrical engineering from Tsinghua University, Beijing, China, in 2004 and 2010, respectively.

He is currently a Postdoctoral Fellow with the University of Michigan, Dearborn, MI, USA. His research interests include battery management systems and high-performance contact and wireless battery chargers for electric vehicles.



Sideng Hu received the Ph.D. degree from Tsinghua University, Beijing, China in 2011.

From August 2011 to August 2013, he was a Post-doctoral Researcher with the University of Michigan, Dearborn, MI, USA. Since September 2013, he has been with the College of Electrical Engineering, Zhejiang University, Hangzhou, China. His research interests include high-frequency dc/dc converters, soft-switching techniques, and vehicle electrification.



Chunting Chris Mi (S'00–A'01–M'01–SM'03–F'12) received the B.S. and M.S. degrees from Northwestern Polytechnical University, Xi'an, China, and the Ph.D. degree from the University of Toronto, Toronto, ON, Canada, all in electrical engineering.

Previously, he was an Electrical Engineer with General Electric Canada, Inc. He is currently a Professor of electrical and computer engineering and the Director of the newly established Department of Energy GATE Center for Electric Drive Transportation,

University of Michigan, Dearborn, MI, USA. He is the author of more than 100 articles. His research interests include electric drives, power electronics, electric machines, renewable-energy systems, and electrical and hybrid vehicles.

Dr. Mi was the Vice Chair and the Chair of the IEEE Southeastern Michigan Section from 2006 to 2007 and from 2008 to 2009, respectively. He was the General Chair of the Fifth IEEE Vehicle Power and Propulsion Conference held in Dearborn on September 6–11, 2009. He was a Guest Editor for the *International Journal of Power Electronics* and an Associate Editor for the *Journal of Circuits, Systems, and Computers* from 2007 to 2009. He has been an Associate Editor for the IEEE TRANSACTIONS ON VEHICULAR TECHNOLOGY, the IEEE TRANSACTIONS ON POWER ELECTRONICS LETTERS, and the IEEE TRANSACTIONS ON INDUSTRY APPLICATIONS, and a Senior Editor for *IEEE Vehicular Technology Magazine*. He serves on the Editorial Board of the *International Journal of Electric and Hybrid Vehicles* and the *Institution of Engineering and Technology Electrical Systems in Transportation*. He received the Distinguished Teaching Award and the Distinguished Research Award from the University of Michigan, Dearborn; the 2007 IEEE Region 4 Outstanding Engineer Award; the IEEE Southeastern Michigan Section Outstanding Professional Award; and the Society of Automotive Engineers Environmental Excellence in Transportation Award.



Ruiqing Ma (M'05) received the B.S. and M.S. degrees in electrical engineering and the Ph.D. degree from Northwestern Polytechnical University, Xi'an, China, in 1985, 1988, and 2007, respectively.

He is currently a Professor of electrical engineering and an Associate Director of the Institute of REPM Electrical Machines and Control Technology, Northwestern Polytechnical University. Since 1993, he has been teaching and conducting research on electric machines and power converters with Northwestern Polytechnical University. His research in-

terests include rare-earth permanent-magnet electric machines drives, power converters, and renewable energy systems.